A&A 599, A9 (2017)
DOI: 10.1051/0004-6361/201629341
© ESO 2017

Astronomy & Astrophysics

Disentangling the ISM phases of the dwarf galaxy NGC 4214 using [C II] SOFIA/GREAT observations[*]

K. Fahrion[1], D. Cormier[1], F. Bigiel[1], S. Hony[1], N. P. Abel[2], P. Cigan[3], T. Csengeri[4], U. U. Graf[5], V. Lebouteiller[6], S. C. Madden[6], R. Wu[7,**], and L. Young[8]

[1] Institut für Theoretische Astrophysik, Zentrum für Astronomie der Universität Heidelberg, Albert-Überle-Straße 2, 69120 Heidelberg, Germany
e-mail: fahrion@stud.uni-heidelberg.de
[2] University of Cincinnati, Clermont College, MCGP Department, Batavia, OH 45103, USA
[3] School of Physics and Astronomy, Cardiff University, Cardiff CF24 3AA, UK
[4] Max-Planck-Institut für Radioastronomie, Auf dem Hügel 69, 53121 Bonn, Germany
[5] I. Physikalisches Institut der Universität zu Köln, Zülpicher Straße 77, 50937 Köln, Germany
[6] Laboratoire AIM, CEA Saclay, Orme des Merisiers, Bât. 709, 91191 Gif-sur-Yvette, France
[7] Department of Astronomy, The University of Tokyo, Bunkyo-ku, 113-0033 Tokyo, Japan
[8] Physics Department, New Mexico Tech, 801 Leroy Place, Socorro, NM 87801, USA

ABSTRACT

Context. The [C II] 158 μm fine structure line is one of the dominant cooling lines in the interstellar medium (ISM) and is an important tracer of star formation. Recent velocity-resolved studies with *Herschel*/HIFI and SOFIA/GREAT showed that the [C II] line can constrain the properties of the ISM phases in star-forming regions. The [C II] line as a tracer of star formation is particularly important in low-metallicity environments where CO emission is weak because of the presence of large amounts of CO-dark gas.
Aims. The nearby irregular dwarf galaxy NGC 4214 offers an excellent opportunity to study an actively star-forming ISM at low metallicity. We analyzed the spectrally resolved [C II] line profiles in three distinct regions at different evolutionary stages of NGC 4214 with respect to ancillary H I and CO data in order to study the origin of the [C II] line.
Methods. We used SOFIA/GREAT [C II] 158 μm observations, H I data from THINGS, and CO(2 $\rightarrow$ 1) data from HERACLES to decompose the spectrally resolved [C II] line profiles into components associated with neutral atomic and molecular gas. We use this decomposition to infer gas masses traced by [C II] under different ISM conditions.
Results. Averaged over all regions, we associate about 46% of the [C II] emission with the H I emission. However, we can assign only ~9% of the total [C II] emission to the cold neutral medium (CNM). We found that about 79% of the total molecular hydrogen mass is not traced by CO emission.
Conclusions. On average, the fraction of CO-dark gas dominates the molecular gas mass budget. The fraction seems to depend on the evolutionary stage of the regions: it is highest in the region covering a super star cluster in NGC 4214, while it is lower in a more compact, more metal-rich region.

Key words. galaxies: dwarf – galaxies: star formation – galaxies: individual: NGC 4214 – ISM: lines and bands

1. Introduction

Star formation proceeds through the contraction and collapse of cold, dense molecular clouds. To study the first stages of star formation, observations of these molecular clouds and the knowledge of their conditions are of great interest. However, direct observations of the most abundant molecule in the cold molecular clouds, H_2, is not possible because the H_2 molecule has no dipole moment and can therefore not be observed in cold and dense environments. Instead, carbon monoxide is traditionally used to study the molecular phase of the interstellar medium (ISM) as CO forms under the conditions prevalent in cold molecular clouds. The lowest ground rotational transition $J = 1 \rightarrow 0$ creates the most prominent line at 2.6 mm

(115.27 GHz), but various other transition lines can be observed as well. The reservoir of molecular hydrogen from which new stars form is usually estimated via the CO-to-H_2 conversion factor α_{CO} (or X_{CO}). Nonetheless, the CO-to-H_2 conversion factor is a controversial quantity as it seems to vary with metallicity (Bolatto et al. 2013; Poglitsch et al. 1995; Cormier et al. 2014; Narayanan et al. 2011; Glover & Mac Low 2011). Furthermore, evidence for hidden molecular hydrogen ("CO-Dark Molecular Gas", Wolfire et al. 2010) has been found not only in the Milky Way (Langer et al. 2014; Planck Collaboration XIX 2011; Grenier et al. 2005), but also in other galaxies (Israel 1997; Madden et al. 1997; Requena-Torres et al. 2016).

These recent studies raise the importance of other tracers that might give insight into the conditions of the molecular content. One of the most promising tracers is the [C II] fine-structure line at 158 μm emitted by singly ionized carbon. [C II] is usually the strongest far-infrared line, representing up to 1% of the continuum emission in the FIR regime (e.g., Stacey et al. 1991; Genzel & Cesarsky 2000; Cormier et al. 2015). Being one

---

[*] Reduced SOFIA/GREAT data are only available at the CDS via anonymous ftp to cdsarc.u-strasbg.fr (130.79.128.5) or via http://cdsarc.u-strasbg.fr/viz-bin/qcat?J/A+A/599/A9
[**] International Research Fellow of the Japan Society for the Promotion of Science (JSPS).

Article published by EDP Sciences

A9, page 1 of 13
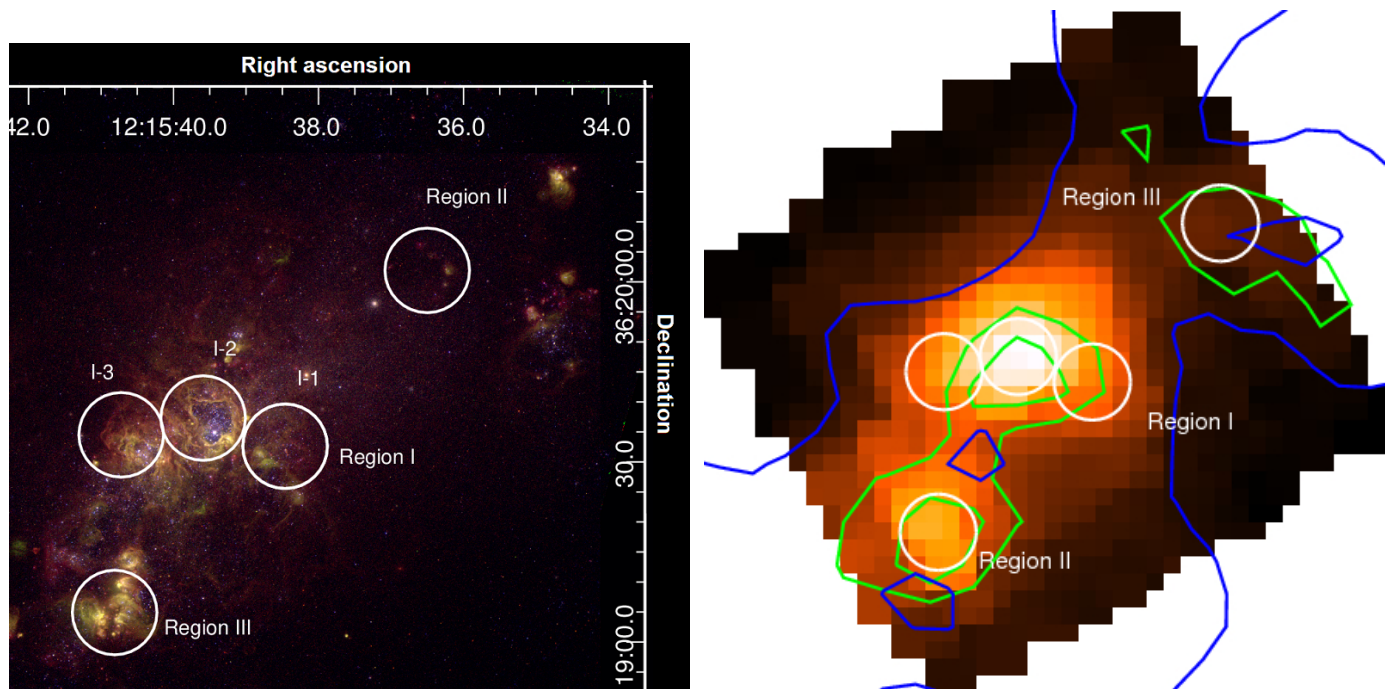
Fig. 1. *Left*: three-color image of the central part of NGC 4214 and pointing positions for SOFIA/GREAT observations. HST *WFC3* filters *F336W* (blue), *F502* (green), and *F657* (red) were used. Credit: NASA/*Hubble*. *Right*: integrated [C II] intensity map observed with *Herschel*/PACS (Cormier et al. 2010). H I (Walter et al. 2008) contours overlayed in blue, CO(2 → 1) (Leroy et al. 2009) contours in green, and SOFIA/GREAT pointings as white circles with a diameter corresponding to 14.1″ (~200 pc). For CO(2 → 1), the contour levels are at 1.2 K km s^{-1} and 2.4 K km s^{-1}. For the extended H I the levels are at 0.23 Jy beam^{-1} km s^{-1} and 0.27 Jy beam^{-1} km s^{-1}. The map covers a 1.6′ × 1.6′ field of view (~1.3 kpc × 1.3 kpc).

of the dominant cooling lines in photon-dominated regions (PDRs, Hollenbach & Tielens 1999) it is often used to study their conditions.

However, because ionized carbon dominates the carbon abundance under most conditions found in the ISM and the [C II] line can be excited by collisions with electrons, atomic, or molecular hydrogen, this line not only traces PDRs, but it can also be found in other phases of the ISM (e.g., Goldsmith et al. 2012). Therefore, the origin of the [C II] line has to be studied in detail in order to use it as a tracer of star-forming regions. Disentangling the different contributions from molecular, ionized, or atomic phases can be done by comparing the spectrally or spatially resolved [C II] emission with tracers of other ISM phases. As high spatial and spectral resolution is needed, this can only be done in nearby objects. So far, integrated line intensities have mostly been used to study star formation in external galaxies, but velocity-resolved observations of the Milky Way and nearby galaxies have become available with the HIFI instrument on *Herschel* and with the GREAT instrument on SOFIA. Constraining the amount of CO-dark molecular gas using [C II] is of particular interest for low-metallicity dwarf galaxies. These galaxies can have very weak CO emission (Schruba et al. 2012; Cormier et al. 2014). At the same time, dwarf galaxies can produce stars at rates that are normally found in starburst galaxies (e.g., Gallagher & Hunter 1984; Hunter et al. 1989). These two observations combined imply that the CO-dark gas may outweigh the CO-bright gas by a large factor. Measuring the CO-dark gas fraction in low-metallicity dwarf galaxies is therefore of key importance for understanding their behavior.

In this paper, we take advantage of the new generation of velocity-resolved [C II] observations from SOFIA/GREAT to disentangle the origin of [C II] emission in NGC 4214.

NGC 4214 is a nearby irregular dwarf galaxy of Magellanic type at a distance of 2.9 Mpc (Maíz-Apellániz et al. 2002; Dalcanton et al. 2009) with low metallicity (log(O/H) + 12 = 8.2, Kobulnicky & Skillman 1996). Owing to its proximity, there is a wealth of ancillary data for NGC 4214. CO(1 → 0) observations showed that NGC 4214 exhibits three distinct star-forming regions in different evolutionary stages (Walter et al. 2001). The left panel in Fig. 1 shows a three-color image of the central part of NGC 4214 with the pointing positions of our SOFIA/GREAT observations of the star-forming regions overlayed as white circles. In the following, we use the labeling of the regions as shown in Fig. 1. The central region (region I) is the most evolved and is also the largest region, containing a super star cluster and several star clusters (Maíz-Apellániz 2001). Bright O stars as well as Wolf-Rayet stars and a Hα cavity are found in this region (MacKenty et al. 2000). Using a UV-optical survey of NGC 4214, Úbeda et al. (2007b) showed that region I is about ~3−4 Myr old. In contrast, the southeastern region, labeled as region II, is only ~2 Myr of age. This region is more compact and contains concentrated gas reservoirs (MacKenty et al. 2000) as well as OB stars and strong Hα emission, which is created in bright Hα knots (Úbeda et al. 2007a; Maíz-Apellániz et al. 1998). Using Hα images and H I velocity data obtained by McIntyre (1997), Thurow & Wilcots (2005) found systematic differences in the kinematics of the ionized gas in region I and II. In the image, the southeastern region is labeled as region III. No star formation is recognizable in this region, but CO emission was found by Walter et al. (2001). Since this region is the least evolved, Walter et al. (2001) suggest that region III will form stars in the future. With these three distinct regions, NGC 4214 offers the possibility of studying the evolution of star formation at low metallicities and in different environments.

Table 1. Fluxes of [C II], H I, and CO for the five SOFIA/GREAT pointing positions.

Region	RA (J2000)	Dec (J2000)	$F([\text{C\,II}])_{\text{PACS}}$ $[10^{-16}\,\text{W m}^{-2}]$	$F([\text{C\,II}])_{\text{GREAT}}$ $[10^{-16}\,\text{W m}^{-2}]$	$F(\text{H\,I})$ $[\text{Jy km s}^{-1}]$	$F(\text{CO(2–1)})$ $[\text{Jy km s}^{-1}]$	$F(\text{CO(1–0)})$ $[\text{Jy km s}^{-1}]$	$R_{\frac{2\rightarrow1}{1\rightarrow0}}$
I-1	12:15:38.48	+36:19:32.4	3.98 ± 0.08	3.54 ± 0.49	0.48 ± 0.01	10.27 ± 2.21	1.77 ± 0.49	1.46 ± 0.52
I-2	12:15:39.61	+36:19:37.1	7.02 ± 0.12	9.62 ± 0.43	0.52 ± 0.01	16.64 ± 2.08	3.14 ± 0.34	1.33 ± 0.22
I-3	12:15:40.74	+36:19:34.3	4.85 ± 0.10	7.27 ± 0.40	0.55 ± 0.01	6.76 ± 1.95	1.12 ± 0.57	1.52 ± 0.89
II	12:15:40.83	+36:19:04.7	5.03 ± 0.09	6.86 ± 0.32	0.49 ± 0.01	19.51 ± 2.34	6.76 ± 0.39	0.76 ± 0.10
III	12:15:36.52	+36:20:01.7	1.18 ± 0.05	2.49 ± 0.62	0.58 ± 0.01	12.09 ± 2.73	3.69 ± 0.70	0.88 ± 0.25

Notes. The last column lists integrated line ratios of CO$(2 \rightarrow 1)$/CO$(1 \rightarrow 0)$ with CO fluxes in K km s^{-1}. To convert from Jy km s^{-1} to W m^{-2}, the fluxes should be multiplied by $a = 10^{-26}\frac{v_0}{c}$, where $a_{\text{H\,I}} = 4.74 \times 10^{-23}$, $a_{\text{CO}(2 \rightarrow 1)} = 7.69 \times 10^{-21}$ and $a_{\text{CO}(1 \rightarrow 0)} = 3.85 \times 10^{-21}$.

We present observations of [C II] emission in three regions of NGC 4214 using the GREAT instrument on board the SOFIA telescope. Our main objective is to extend the few studies of CO-dark gas in galaxies by decomposing the spectrally resolved [C II] emission of NGC 4214 into fractions associated with the atomic and the molecular hydrogen gas content. In particular, our new observations allow us to determine which fraction of the [C II] emission can be associated spectrally with the CO-emitting gas and, in turn, which fraction is too far removed in velocity-space to be physically linked directly to the cold dense gas detected in CO. In Sect. 2 we describe the data, in Sect. 3 we describe our decomposition method with its results, and in Sect. 4 we present the associated gas fractions and masses. Our analysis is summarized and discussed in Sect. 5.

2. Data

2.1. [C II] data

2.1.1. SOFIA data

The [C II] emission at 1900.54 GHz (158 μm) was observed in NGC 4214 using the L2 band of the GREAT instrument (Heyminck et al. 2012) on board the airborne Stratospheric Observatory for Infrared Astronomy (SOFIA; Young et al. 2012). Observations were performed as part of observation cycle 2 in May 2014 and January 2015 with a half-power beam width of 14.1″ (∼200 pc) and 1.16 km s^{-1} velocity resolution. Five positions in NGC 4214 were observed in the three main star-forming regions (Fig. 1; the coordinates can be found in Table 1). SOFIA has a pointing accuracy of ∼0.5″. The data were processed with the eXtended bandwidth Fast Fourier Transform Spectrometer (XFFTS) and the standard GREAT calibrator (Guan et al. 2012). The data were calibrated to antenna temperature scale ($\eta_{\text{f}} = 0.97$) and to the main beam temperature scale ($\eta_{\text{mb}} = 0.65$−0.69 for L2). We converted the data from main beam temperature scale to Jansky using a conversion factor of 585 Jy/K.

Before averaging the spectra, the baseline was removed using a polynomial of first order except in a few spectra from May 2014 where third-order polynomials were used. Data reduction was done using the CLASS software[1]. For further analysis we rebinned the data to 2.6 km s^{-1} resolution. The fluxes reported in Table 1 were calculated by direct integration of the rebinned spectra between 270 and 330 km s^{-1}, except for region III where we used channels between 240 and 330 km s^{-1}. These ranges were chosen based on the line widths also observed in CO and H I.

[1] http://www.iram.fr/IRAMFR/GILDAS

2.1.2. Herschel/PACS

NGC 4214 was also observed in the [C II] line with the PACS spectrometer (Poglitsch et al. 2010) on the *Herschel* Space Observatory (Pilbratt et al. 2010). The data were originally presented in Cormier et al. (2010) and reprocessed with the PACS spectrometer pipeline of the *Herschel* interactive processing environment (HIPE) v14.2. The PACS map covers a 1.6′ × 1.6′ field of view with a spatial resolution of 12″. Figure 1 shows the integrated intensity map observed with *Herschel*/PACS in the right panel. We compare the fluxes of GREAT and PACS for the regions observed with both instruments. To this end, the PACS map was convolved with a Gaussian kernel to the angular resolution of SOFIA/GREAT data and aperture photometry was applied to compute the fluxes shown in Table 1. For both [C II] datasets, the emission is strongest in pointing I-2 in the central region of NGC 4214 where the super star cluster is located and weakest in region III. The *Herschel*/PACS and SOFIA/GREAT fluxes are in relatively good agreement (within 40%) in regions I and II. In region III, the GREAT flux is about two times higher than the PACS flux, but [C II] is not detected at high significance in this region.

2.2. [H I] data

NGC 4214 was observed in the CO$(1 \rightarrow 0)$ transition line with the Caltech OVRO millimeter interferometer by Walter et al. (2001). The data have a velocity resolution of 1.30 km s^{-1} and the half-power beam width is 6.4″ × 5.7″.

NGC 4214 was also included in the HERA CO-Line Extragalactic Survey (HERACLES; Leroy et al. 2009). The CO$(2 \rightarrow 1)$ line at 230.54 GHz (1.3 mm) was observed with a half-power beam width of 13″ and 2.6 km s^{-1} velocity resolution. Although the spectral resolution is higher for the OVRO CO$(1 \rightarrow 0)$ data, we used CO$(2 \rightarrow 1)$ to distinguish the origin of [C II] emission because the velocity range covered by the OVRO data is narrower, ranging only from 262 to 343 km s^{-1}, while the H I emission is more extended than this. This can be seen in Fig. 2. A second disadvantage of using the OVRO interferometry data is that we might miss extended CO emission. However, in the low-metallicity environment of NGC 4214, we do not expect a significant amount of extended emission.

Nonetheless, we want to investigate the possibility of missing CO in the OVRO observations and thus calculate the flux ratios of CO$(1 \rightarrow 0)$ and CO$(2 \rightarrow 1)$. Table 1 provides the flux ratios (in K km s^{-1}) for both OVRO and HERACLES datasets in each region. To calculate this quantity, we convolved the OVRO CO$(1 \rightarrow 0)$ data to the angular resolution of the HERACLES observation and integrated by summation over the channels.
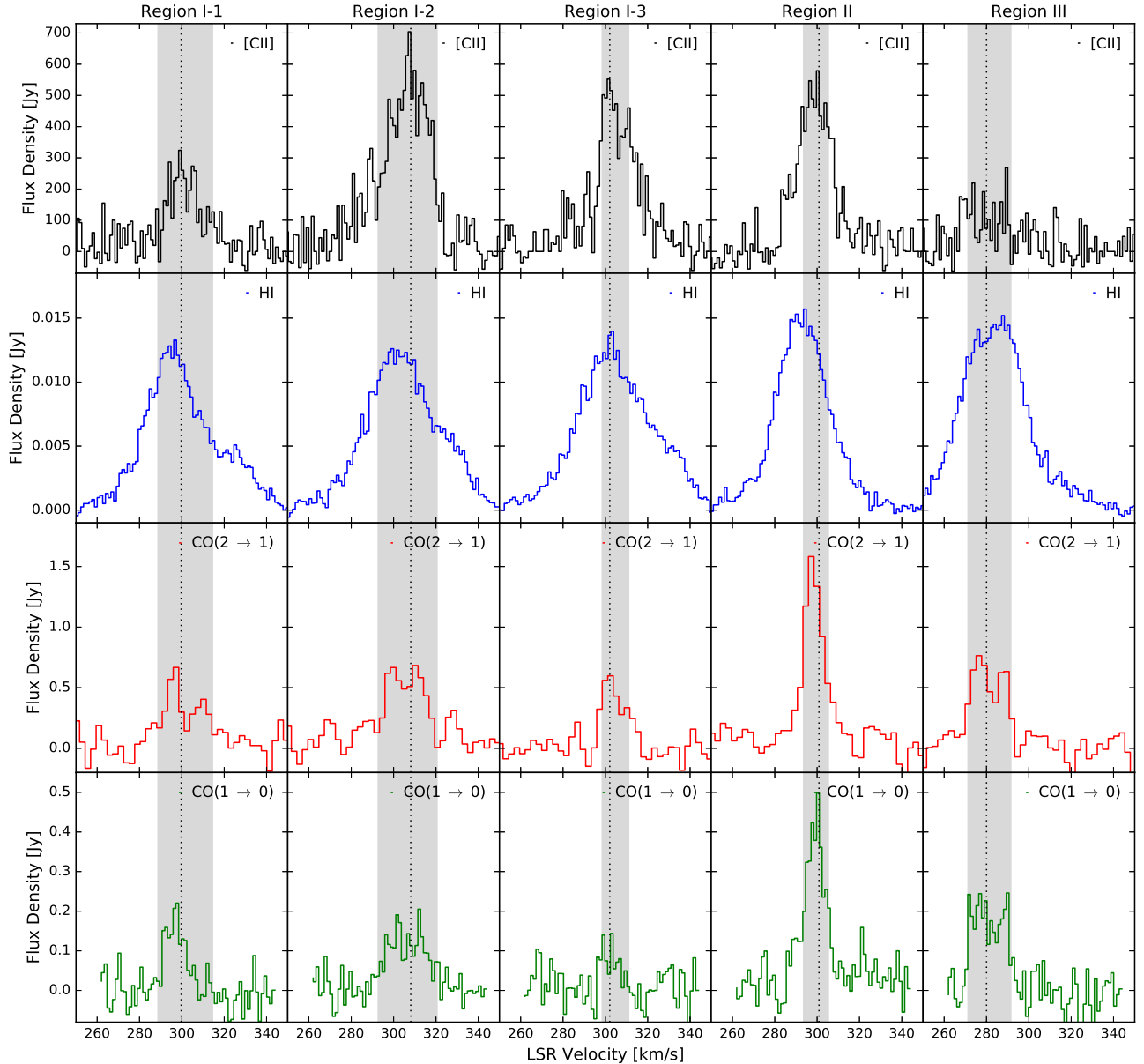
Fig. 2. Emission spectra of SOFIA/GREAT [C II] and ancillary CO and H I in the five positions in NGC 4214. The spectra shown are based on the data that were spatially convolved with Gaussian kernels to the resolution of the SOFIA data (14″). The vertical lines indicate the channel with maximum [C II] emission, except for region III where it indicates the center of the broad profile. The gray-shaded areas indicate the FWHM ranges around the CO-peak positions. The original velocity resolutions shown here are 1.16 km s^{-1}, 1.29 km s^{-1}, 2.6 km s^{-1}, and 1.30 km s^{-1} for [C II], H I, CO(2 → 1), and CO(1 → 0), respectively.

Especially in region I, the values are higher than the typical ratios of 0.8 (Braine et al. 1993), but overall they agree within the uncertainties. The values seem reasonable, but we note that the OVRO data may be subject to missing flux (zero-spacing) so that the ratios formally represent an upper limit of the true ratio. However, given the strong radiation fields from ongoing star formation – in particular in regions I and II – and the low-metallicity, we do not expect a diffuse CO component.

We used H I data from The HI Nearby Galaxy Survey (THINGS; Walter et al. 2008) which performed observations of the atomic hydrogen content in nearby galaxies using the 21 cm (1.4204 GHz) line of atomic hydrogen with a half-power beam width of 14.69″ × 13.87″ and 1.29 km s^{-1} spectral resolution.

Table 1 lists the fluxes for H I, CO(2 → 1), and CO(1 → 0) in all regions. The fluxes were derived after convolving the CO data to the angular resolution of SOFIA/GREAT. For the

CO lines, we chose channels between 270 and 330 km s^{-1} for integration and for H I we take the channels between 250 and 350 km s^{-1}. In region III, however, we set the integration range to 240−300 km s^{-1} for both CO and H I spectra. The H I fluxes are almost constant over the regions, while the CO fluxes have their maximum in region II.

2.3. Description of the spectra

The spectra of [C II], H I, CO(2 → 1), and CO(1 → 0) in the five regions observed by SOFIA/GREAT are shown in Fig. 2.

By fitting Gaussians, we find that the [C II] emission lines have widths of ~20 km s^{-1} and are centered at about 300 km s^{-1}, except in region III where the data show weak [C II] emission

Table 2. Parameters of the Gaussian fitting of the H I and CO spectra.

Region	H I				CO($2 \rightarrow 1$)	
	$p_{HI,1}$ [km s^{-1}]	$FWHM_{HI,1}$ [km s^{-1}]	$p_{HI,2}$ [km s^{-1}]	$FWHM_{HI,2}$ [km s^{-1}]	p_{CO} [km s^{-1}]	$FWHM_{CO}$ [km s^{-1}]
I-1	295.7	29.1	327.1	21.5	301.6	25.8
I-2	302.7	35.0	331.4	15.5	306.6	27.8
I-3	302.7	36.2	333.4	18.7	304.8	12.5
II	293.6	28.7	–	–	299.5	11.7
III	284.0	35.3	–	–	281.4	20.2

Notes. Peak positions p and FWHMs ($=2.35\sigma$). Two Gaussians were fitted to the H I spectra of the pointings in region I.

centered at lower velocities of $\sim$280 km s^{-1} with widths of $\sim$30 km s^{-1}.

The H I profiles are broader (about 30 km s^{-1}). Again, in region III the peak position is at lower velocities, but in regions I-1, I-2, and II we also find the peak position shifted to slightly lower velocities compared to the [C II] spectra.

We note that the CO emission in both transition lines is clearly strongest in region II with a width of $\sim$15 km s^{-1}, while the other regions show widths between 20 and 25 km s^{-1}. The spectra peak at $\sim$300 km s^{-1} except for region III where the velocity is again lower. The spectra of CO($2 \rightarrow 1$) and CO($1 \rightarrow 0$) have similar shapes. However, in regions I-1, I-2, and I-3 there are some features to the right and left of the central peak that are only visible in one of the two datasets.

Table 1 shows that the H I fluxes are almost constant throughout the five regions, as is also indicated by the spectra. We find that the CO emission is weak compared to [C II] with flux ratios of [C II]/CO($1 \rightarrow 0$) between 2×10^4 and 17×10^4 with a clear minimum in region III and the maximum in region I-2 (see also Cormier et al. 2010).

3. Decomposition of [C II] spectra

The main goal of this work is to determine how much of the [C II] emission traces the dense molecular material that is also probed by CO. If it were a one-to-one tracer, the velocity profiles of [C II] and CO would be similar. However, as Fig. 2 already shows, the [C II] profiles in NGC 4214 show broader wings that are not seen in CO. To determine the maximum amount of [C II] that can be associated with the molecular phase and to investigate the origin of these wings, we decompose the spectrally resolved [C II] observations into contributions correlated with H$_2$ (as traced by CO($2 \rightarrow 1$)) and H I. In doing so, we assume that CO($2 \rightarrow 1$) and H I trace material with uniform conditions. The consideration of atomic gas with different conditions is discussed in Sect. 5.1.2.

We decompose our [C II] spectra into a linear combination of H I and CO in two different ways. The first approach (channel method) uses the CO and H I spectra directly by adding them manually (see Appendix A). The second approach uses Gaussian fits for the decomposition, as described in the following. Although neither method shows striking inconsistencies, we focus on the Gaussian fit method as it appears to be more robust.

3.1. Description of the Gaussian fit method

We use Gaussian fits to decompose the [C II] spectra. In this approach, we first fit H I and CO($2 \rightarrow 1$) spectra independently with Gaussians. We fit two independent Gaussian curves to the

H I spectra in region I as there seem to be two distinct components (see Sect. 2). For CO($2 \rightarrow 1$), we only use one component because of the lower signal-to-noise ratio. Table 2 lists the fitted peak positions and widths (FWHM of the Gaussian curves) for the H I and CO spectra in the five regions in NGC 4214. Figure 3 shows that two Gaussians reproduce the H I data well in the pointings of region I; however, the parameters of the second Gaussian are less well constrained. We note that the first component of H I in region I has the same width as the H I spectra in region II and III indicating that the second component might be emission on the line of sight not connected to the star-forming region. The CO($2 \rightarrow 1$) spectrum in region I-1 is fitted with a very broad Gaussian ($FWHM \approx 26$ km s^{-1}), whereas the CO($1 \rightarrow 0$) is fitted with a FWHM of ≈ 11 km s^{-1}. We approximate the CO width in region I-1 for the latter analysis to be 18 km s^{-1}, the average FWHM of the original fitting of the CO($2 \rightarrow 1$) and CO($1 \rightarrow 0$) spectra. We discuss how changing the FWHM in this region to the individually fitted values (11 and 26 km s^{-1}) affects the decomposition results in the following section. In the other regions fitting the CO($1 \rightarrow 0$) and CO($2 \rightarrow 1$) spectra yields comparable widths.

We then normalize the [C II] spectra to their maxima and fit them with Gaussians of the form

$$g(v) = A_1 \exp\left(-\frac{(v - p_{HI,1})^2}{2\sigma_{HI,1}^2}\right) + A_2 \exp\left(-\frac{(v - p_{HI,2})^2}{2\sigma_{HI,2}^2}\right)$$
$$+ B \exp\left(-\frac{(v - p_{CO})^2}{2\sigma_{CO}^2}\right). \tag{1}$$

The peak positions p and widths σ are taken as fixed parameters determined by the above-mentioned fits. The coefficients A_i (H I amplitudes) and B (CO) are used as free parameters for the fit. In region II and III, we use only one H I term. In region III, we rebin the [C II] spectrum to a resolution of 5 km s^{-1} to improve the signal-to-noise ratio.

3.2. Results

Figure 4 shows the [C II] spectra in black with the best fitting curves overlaid in red. The fitted amplitudes and their uncertainties are given in Table 3. The stated uncertainties are the 1σ errors from the fitting procedure. In the three pointings of region I, we find that the best fit is provided when the contribution of the second H I component is close to zero. This supports our assumption that this second component may not be connected to the star-forming region while the [C II] emission is.

In addition, we note that the CO amplitudes are higher than the sum of H I amplitudes in all regions except for region III, where the uncertainties are high. The [C II] spectra are best decomposed when using large fractions of the CO($2 \rightarrow 1$) spectra
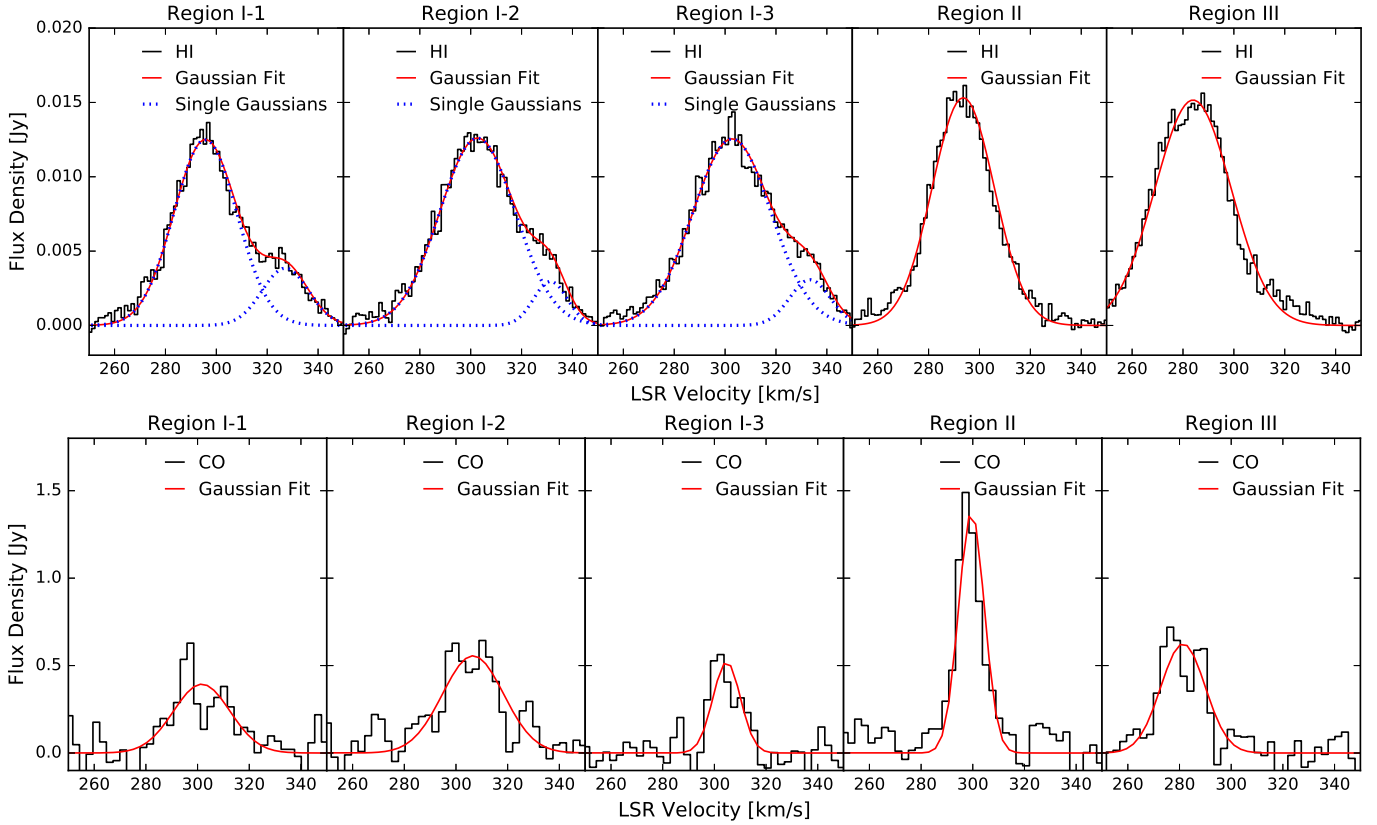
Fig. 3. *Upper row*: H ɪ spectra of the five pointings in NGC 4214 fitted with Gaussian curves. For the spectra in region I, we use two Gaussians (single components in blue). *Bottom row*: CO(2 → 1) fitted with single Gaussian curves.
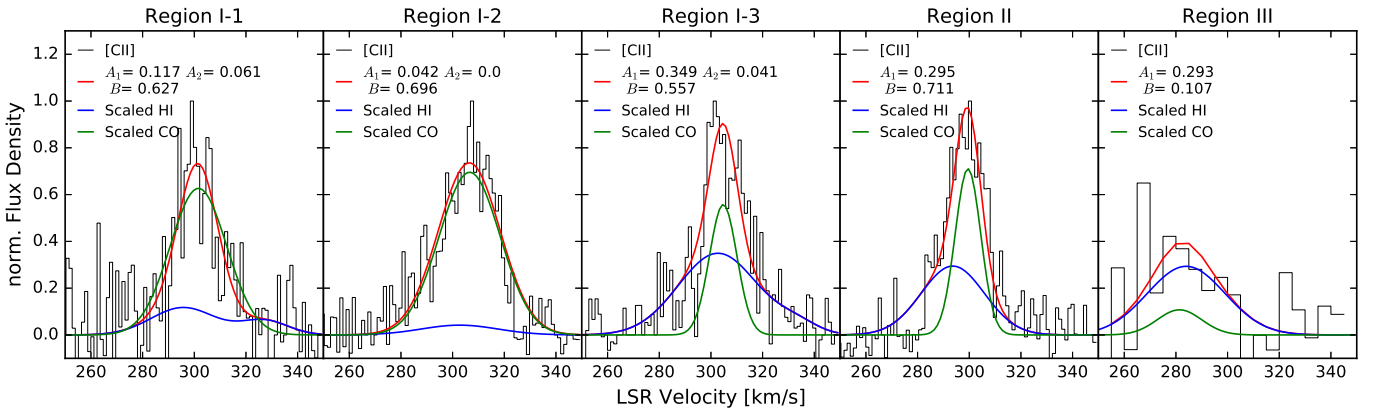
Fig. 4. Gaussian fit method. [C ɪɪ] spectra in the five pointings fitted with Gaussian curves as described by Eq. (1). In region II and III we only fit two Gaussian curves, but in the pointings of region I we use two H ɪ components. The [C ɪɪ] spectra in region III was rebinned to 5 km s⁻¹.

Table 3. Results from the Gaussian fit decomposition.

Region	A_1 H ɪ	A_2 H ɪ	B CO	$I_{[C II]}(CO)/I_{[C II]}$ central value	1σ interval
I-1	0.12 ± 0.08	0.06 ± 0.05	0.62 ± 0.10	77.4%	65−85%
I-2	0.04 ± 0.10	0.00 ± 0.04	0.70 ± 0.11	93.0%	85−100%
I-3	0.35 ± 0.04	0.04 ± 0.04	0.56 ± 0.08	34.3%	25−45%
II	0.29 ± 0.04	–	0.71 ± 0.06	49.5%	40−60%
III	0.29 ± 0.11	–	0.18 ± 0.24	17.5%	0−30%

Notes. A_1, A_2 and B are the coefficients of the components (Eq. (1)). Columns 5 and 6 list the central values and 1σ intervals of the fraction of [C ɪɪ] intensity associated with CO (see Sect. 3.2). The intensity fractions associated with H ɪ are the remaining fraction of the [C ɪɪ] intensity.

in agreement with the scaling coefficients used in the channel method (Appendix A). To verify that the Gaussian fits recover the [C II] fluxes, we compare the velocity integrated fluxes of the original [C II] data with the combined Gaussians using the same velocity ranges as before. The ratios of Gaussians and direct integration are very close to unity and therefore our fits recover all of the [C II] emission.

With the spectral decomposition of [C II] emission determined in this way, we calculate the fractions of [C II] intensity associated with CO($2 \rightarrow 1$) and H I. Each fraction is determined as the ratio between the integrated [C II]-fitted profiles and the accordingly scaled H I and CO spectra that were used in the decomposition. Simply put, we compare the areas below the red curves (final fit) in Fig. 4 to the areas below the green and blue curves (corresponding H I and CO contributions to the final fit). The [C II] intensity fractions associated with CO($2 \rightarrow 1$) are listed in Table 3. In region I-2, we find almost no contribution from the H I, and the CO($2 \rightarrow 1$) contribution to the [C II] flux is also higher than the H I contribution in region I-1. In region II, the parts are almost equally split. In region III, we can only associate a rather small fraction of CO emission with the [C II].

We validate the uncertainties on the amplitudes given by the IDL routine GAUSSFIT in the following manner. We vary the CO amplitude from 0.3 to 0.9 in steps of 0.1 and re-fit the H I amplitude. For each chosen CO amplitude, we estimate the goodness of the fit by considering the residuals (signal − fit) normalized by the noise level of the [C II] data. We calculate the χ^2 by summing these residuals over the channels between 280 and 320 km s^{-1}. The 1σ interval that we find corresponds well with the uncertainties given by the fitting procedure. This range of amplitudes is then translated into uncertainties on the intensity fractions (Col. 5 of Table 3). We find that these uncertainties are about ±10%, except for region III where they are at least ±20%. For region I-1, we also explore the sensitivity of the results to the value of the CO FWHM because the two available CO lines yield substantially different values. When using 26 km s^{-1}, i.e., the value derived from the CO($2 \rightarrow 1$), we obtain a poor fitting result because the CO($2 \rightarrow 1$) line is broader than the observed [C II] line. As a result, the wings and the peak in the [C II] cannot be reproduced at the same time. When using the FWHM determined from CO($1 \rightarrow 0$), we obtain a reasonable decomposition with a CO amplitude of 0.55 and a residual comparable to when using the average FWHM. This results in a CO-associated intensity fraction of $(56 \pm 10)\%$, a value around 20% lower than that given in Table 3 calculated with the average FWHM (18 km s^{-1}). We note that the maximum CO percentage provides a hard limit on the amount of [C II] that can be associated with CO. The lower limit is less strict because it depends on the nature of the H I-emitting gas (see Sect. 5.1.2). The H I profiles might contain narrow and broad components that we cannot separate owing to the limited spatial resolution of the H I observations.

The quality of the input spectra that define the Gaussian components plays an important role in our method. The uncertainties of our results could be further reduced with deeper CO observations. This is particularly true for region I-1, but is true for the other regions as well.

4. Gas masses from different tracers

4.1. C$^+$ column densities and associated gas masses

The decomposition described in the previous section divides the [C II] emission into fractions associated with H I and CO($2 \rightarrow 1$) emission. We find that the CO fraction tends to be larger;

however, the [C II] profiles show both narrow and broad components. Assuming different sets of conditions in the ISM, we calculate the gas masses that these components would correspond to. In principle, at our spatial resolution ($14'' \sim 200$ pc), the ISM should contain ionized gas, cold neutral medium (CNM), warm neutral medium (WNM), and dense neutral/molecular gas (PDR). While the narrow components in the [C II] profiles can be associated with the PDR, the broad components can correspond to ionized gas, WNM, and/or CNM.

We neglect the contribution from ionized gas because of a previous study of NGC 4214 by Dimaratos et al. (2015). They performed a self-consistent radiative transfer modeling of the H II gas and PDR in regions I and II of NGC 4214 using a suite of mid-IR and far-IR lines. They find that the H II region models contribute only a small percent of the [C II] emission. Using the [N II] lines at 122 μm and 205 μm, they also estimate the contribution of a diffuse ionized phase to the [C II] emission to be less then 8%.

We study the extended component, i.e., the H I-associated [C II] flux, as well as the CO-matched dense material by calculating gas masses (corresponding to H I or H$_2$ masses) assuming different sets of ISM conditions (see Table 4). None of the quoted masses includes helium.

We calculate C$^+$ column densities from the observed intensity $I_{[CII]}$ following Madden et al. (1997):

$$
\begin{aligned}
N(C^+) &= 1.06 \times 10^{15} \frac{\int F_\nu d\nu \,[\text{Jy km s}^{-1}]}{\Theta['']^2} \\
&\times \left(\frac{1 + 2\exp(-91.3\,\text{K}/T) + n_{\text{crit}}/n}{2\exp(-91.3\,\text{K}/T)} \right).
\end{aligned}
\tag{2}
$$

Here T is the kinetic gas temperature in Kelvin, and n the density and n_{crit} the critical density of the main collision partner of C$^+$ both in cm^{-3}. We assume that all of the carbon is ionized in the CNM, WNM, and in the PDR, and that the [C II] line is excited by collisions with atomic hydrogen in the phases associated with H I emission and by collisions with molecular hydrogen in the PDR (see Table 4). We use the intensity fractions from Table 3 to scale the column density according to the ISM phase that is considered.

For the abundance of ionized carbon, $X_{C^+/H} = 5.07 \times 10^{-5}$ is used in region I and $X_{C^+/H} = 7.24 \times 10^{-5}$ is used in region II (Kobulnicky & Skillman 1996). There is no measurement for region III, so we used the lower value since this region is thought to be less evolved.

We then calculate the gas masses traced by [C II] and associated with CO and H I by adapting Eq. (3) from Pérez-Beaupuits et al. (2015) to our data. We assume a beam filling factor of 1:

$$
M_{\text{gas}}[M_\odot] = 3.16 \times 10^{-16} \frac{N(C^+)}{X_{C^+/H}}.
\tag{3}
$$

The resulting gas masses are reported in Table 4 using intensity fractions with uncertainties from Table 3. We emphasize that these masses are theoretical values assuming that the H I and CO-associated fractions of the [C II] intensity originate from regions of uniform ISM conditions. We discuss these model values further in Sect. 5. The gas masses are sensitive to the assumed ISM conditions. For example, changing the CNM temperature from 80 to 100 K results in CNM-associated gas masses that are reduced by 20% compared to the values given in Table 4. By changing the electron density from 100 to 200 cm^{-3}, the gas mass is about half of the reported value. Similarly, changing the

Table 4. Assumed sets of conditions for ISM phases used to calculate [C II]-associated gas masses, and observed H I and H$_2$ masses.

			CNM	WNM	PDR CO
Collision partner of C$^+$			H	H	H$_2$
T [K]			80	8000	150
n [cm^{-3}]			100	0.5	10^4
$n_{\rm crit}$ [cm^{-3}]			3000	1600	6100

Region	$M_{\rm HI}$ [$10^5\,M_\odot$]	$M_{\rm H_2}$ [$10^5\,M_\odot$]	$M_{\rm gas}([{\rm C\,II}]_{\rm H\,I,\,CNM})$ [$10^5\,M_\odot$]	$M_{\rm gas}([{\rm C\,II}]_{\rm H\,I,\,WNM})$ [$10^7\,M_\odot$]	$M_{\rm gas}([{\rm C\,II}]_{\rm CO,\,PDR})$ [$10^5\,{\rm M_\odot}$]
I-1	9.30	1.94	$23.16^{+9.01}_{-9.37}$	$7.57^{+2.95}_{-3.07}$	$6.88^{+0.94}_{-0.90}$
I-2	10.11	3.12	$4.25^{+20.73}_{-4.25}$	$1.39^{+6.78}_{-1.39}$	$24.58^{+0.43}_{-2.08}$
I-3	10.62	1.27	$117.39^{+14.72}_{-23.03}$	$38.40^{+4.82}_{-7.53}$	$7.14^{+2.30}_{-1.47}$
II	9.36	3.65	$60.36^{+14.47}_{-10.46}$	$19.74^{+4.73}_{-3.43}$	$6.44^{+1.05}_{-1.45}$
III	11.20	2.42	$53.33^{+11.31}_{-8.08}$	$17.44^{+3.70}_{-2.64}$	$1.13^{+0.81}_{-1.13}$

Notes. We present the observed H I and H$_2$ masses and compare them to theoretical values of the gas mass calculated from the H I- or H$_2$-associated components of the [C II] intensities under the assumption that all of the H I- or CO-associated [C II] emits from an ISM phase with the conditions stated above. The uncertainties result from the uncertainties given in Table 3. PDR conditions are from Dimaratos et al. (2015), critical densities from Goldsmith et al. (2012).

PDR temperature to 100 K, the theoretical mass is reduced by 18%. By decreasing the assumed PDR density by a factor of 2 to 5000 cm^{-3}, the resulting mass is reduced by 20%. However, owing to the inherently high density in this phase, the masses are less sensitive to an increase in the density. If the density is increased to 10^5 cm^{-3}, the mass increases by 25%. We discuss the sensitivity to the assumed parameters further in Sect. 5.1.

4.2. Gas masses traced by H I and CO

In addition to the gas masses traced by [C II], we also calculate the atomic and molecular gas masses using the H I and CO(1 → 0) intensities directly (Table 4).

The H I mass is calculated using the relation

$$M_{\rm HI}[M_\odot] = 2.36 \times 10^5\,(D[{\rm Mpc}])^2 \int F_\nu {\rm d}v\,[{\rm Jy\,km\,s^{-1}}]. \qquad (4)$$

To calculate the molecular gas mass from CO(1 → 0) emission, we use Eq. (2) from Bolatto et al. (2013)

$$M_{\rm H_2}[M_\odot] = \frac{\alpha_{\rm CO}}{1.36} L_{\rm CO(1\to0)}, \qquad (5)$$

where $\alpha_{\rm CO} = 4.3\,M_\odot({\rm K\,km\,s^{-1}\,pc^2})^{-1}$ is the Galactic value of the CO-to-H$_2$ conversion factor and $L_{\rm CO(1\to0)}$ is expressed in K km s^{-1} pc^2. The factor of 1.36 is the helium contribution that we do not consider here. Table 4 lists the H I and H$_2$ masses calculated from H I and CO emission directly.

While the H I mass distribution is almost constant throughout the regions, the values for H$_2$ masses differ from region to region by up to a factor of 2; the maximum is found in region II. We find ratios of $M_{\rm H_2}$ to $M_{\rm HI}$ of ~0.2. These ratios are higher than the 0.02 found by Leroy et al. (2009) for the whole galaxy because we only study the star-forming regions and therefore only include small fractions of the extended H I.

5. Discussion

5.1. [C II] emission from different ISM phases

We showed in our analysis that the [C II] velocity profiles do not have the same shapes as the CO profiles, but they show broad wings that can be reproduced by H I. We want to understand what this means in terms of how reliably [C II] traces the molecular phase and what the origin of these broad wings might be. With our decomposition and the calculated model gas masses (Table 4), we can explore this issue.

5.1.1. Molecular gas

The [C II] gas mass associated with the dense PDR (traced by CO emission) reaches its maximum in region I-2 and its minimum in region III. In the other regions the mass is almost constant. Except for region III, we find that the [C II] emission traces 3−8 times more mass than CO.

We can estimate how much of the molecular mass is CO-dark by comparing the molecular gas mass found with [C II] emission assuming PDR conditions with the molecular gas mass directly determined from CO(1 → 0) observations (Cols. 6 and 3 in Table 4, respectively). We calculate the CO-dark molecular mass fraction as the molecular mass derived from [C II] divided by the total molecular mass (from CO and [C II]). In regions I-1, I-2, and I-3, the fraction of total molecular gas mass only seen by [C II] is high with $(78 \pm 13)\%$, $(89 \pm 10)\%$, and $(85^{+15}_{-25})\%$, respectively, suggesting a large amount of CO-dark-H$_2$ gas extended over region I as is expected in low-metallicity environments. The errors quoted here result from the 1σ uncertainties in the decomposition. Since Maíz-Apellániz et al. (1999) and MacKenty et al. (2000) found that region I is resolved into two different regions around two massive star clusters, it is not surprising that we find different fractions in the three pointings. We note, that region I-2 covers the super star cluster (cluster A, see Maíz-Apellániz et al. 1999; or Maíz-Apellániz 2001), while a second cluster (labeled B) is covered by pointing I-3. While region I has an age of 3−4 Myr (Úbeda et al. 2007b), region II is a more compact and younger (~2 Myr) star-forming region with

higher metallicity (by ~0.1 dex; Kobulnicky & Skillman 1996). In region II, we report that $(64 \pm 20)\%$ of the total molecular mass is found with [C II] emission. This value is lower than the those found in region I and might be explained by increased dust shielding, as indicated by the slightly higher metallicity and less porous ISM structure of this younger region. On average, around 79% of the total molecular mass is CO-dark.

The gas mass found in CO slightly exceeds the mass found by [C II] in region III. We can therefore make no statement about the CO-dark gas in this region owing to a combination of an uncertain decomposition and low [C II] intensity. Region III is the least evolved region with no visible star formation.

We note that the [C II]-associated gas masses vary with the assumed conditions. While small deviations from the assumed ISM conditions could reduce the CO-dark fractions, we find average PDR densities of ~500 cm^{-3} or temperatures of ~35 K are needed to explain the observed H$_2$ masses without any CO-dark gas. Those conditions are not in agreement with the PDR analysis of Dimaratos et al. (2015). These are strong arguments in favor of a massive CO-dark gas phase.

Instead of masses, we can also quote fractions of total [C II] intensity assigned to the CO-dark phase. In region II, we can assign $(33 \pm 9)\%$ of the total [C II] intensity to this phase. In regions I-1, I-2, and I-3 we find values of $(58 \pm 11)\%$, $(87 \pm 12)\%$, and $(32 \pm 12)\%$, respectively.

5.1.2. Atomic gas

For the atomic gas, we have estimated gas masses assuming WNM and CNM conditions. In the WNM case, very large masses, on the order of $10^8\ M_\odot$, would be required in order to explain the observed [C II] emission. Given that these are much larger than the observed H I masses from the 21 cm line, only ~1% of the observed [C II] intensity can arise from the WNM. In their study of the Milky Way, Pineda et al. (2014) also find no significant contribution of the WNM to the [C II] emission.

Nonetheless, the WNM can make up a significant fraction of the total atomic content (e.g., Kulkarni & Heiles 1987; Heiles & Troland 2003), especially at large velocities due to high temperatures. The widths of the H I profiles that we observe could therefore be caused by the WNM. In principle, it might be better to first subtract any WNM contribution to the H I line as the [C II] line is less sensitive to this warm phase. However, it is not easy to determine what causes the broad H I profile. Sellwood & Balbus (1999) and Tamburro et al. (2009) argue that turbulence stirred by magnetorotational instability can also lead to broad line widths. Moreover, there could also be significant substructure within the telescope beam. To constrain any contribution from the WNM, further H I observations with higher spatial resolution would be needed.

Even if we assume that the H I-associated [C II] originates from the CNM, the corresponding masses exceed the upper limits given by the H I observations directly. We find that between 4 and 10% of our total [C II] intensity can arise from the CNM in order to reproduce the H I 21 cm masses. In region III, we can assign $(17 \pm 6)\%$ of the [C II] emission to the CNM. In a study of the metal-poor irregular galaxy IC10, Madden et al. (1997) assigned about 10% of [C II] emission to the CNM (and ~10% to the ionized medium) in agreement with our results. This indicates that the H I-associated [C II] not only emits from the CNM, but also from a denser phase. To match the H I masses, we would need densities of about 1000 cm^{-3} on average when assuming temperatures of 80 K and a critical density of 3000 cm^{-3}. We note that it is not realistic that all the H I-associated [C II] emits

under these conditions, but it indicates that our CNM is not dense enough to be the sole origin of the broad wing component in the [C II] profiles. Furthermore, such high densities are unlikely as they would presumably appear as narrow wings, and not the broad wings that are seen in the [C II]. The true nature of these wings is not clearly understood.

Parts of the H I-associated [C II] might come from the same dense PDR regions that are also traced by CO. This dense component of the H I profile should have a similar velocity profile to CO, and as Fig. 2 shows, it would be possible to fit a dense CO-associated component to the H I near the peak. Therefore, when using only the three tracers discussed in this work, it becomes difficult to separate dense and extended components. Our findings show that further studies with additional, clearly separable tracers of molecular and atomic gas phases would be needed to resolve this issue.

5.2. Comparison with other sources

Previous studies on star-forming regions and ISM conditions in nearby galaxies have shown a complex origin of [C II] emission. Requena-Torres et al. (2016) performed a study of carbon gas with high spatial and velocity resolution in low-metallicity star-forming regions N 66, N 25 + 26, and N 88 of the Small Magellanic Cloud (SMC). While N 66 is an extended (100−150 pc) gas cloud with bright core, N 25 and N 26 are part of a group of H II regions and N 88 is compact (~1 pc) source in the SMC wing. They found [C II] emission profiles that are up to 50% wider in velocity than the corresponding CO profiles. They suggest that the gas traced with CO is embedded in a larger molecular cloud only seen by [C II] in the observed region. From studies on the C$^+$ column densities they concluded that most of the [C II] emission originates from CO-dark molecular gas. Only a few percent are contributed by either ionized and atomic hydrogen. The transition lines of CO only trace between 5 an 40% percent of the molecular gas found in the observed regions.

Like the SMC, the LMC provides spatially and velocity-resolved observations of low-metallicity environments. Okada et al. (2015) studied the star-forming region N 159 in the LMC with [C II] SOFIA/GREAT observations in comparison with different CO transition lines at a spatial resolution of ~4 pc. With a similar approach using Gaussian curves to fit the [C II] lines they found that the fraction of the [C II] that cannot be attributed to the gas traced by CO is 20 % around the regions with maxium CO emission and up to 50 % in the area between the CO cores. Additionally, they estimate the contribution from ionized gas to be ≤15% in the whole observed region. While these results were obtained with a [C II] map, we only studied regions with strong CO emission and find that the fraction of [C II] emission associated with CO differs greatly from region to region. Averaged over all regions we can associate ~54% with the CO emission in NGC 4214.

Braine et al. (2012) studied M 33 in the [C II] line with *Herschel*-HIFI at a spatial resolution of about 50 pc and also found that the [C II] lines are broader than the CO lines by about 50% but narrower than H I. Spatially resolved [C II] PACS maps (Mookerjea et al. 2011) showed that there is little spatial correlation between [C II] and CO or H I.

The difference in [C II] and CO line profiles is not as striking as in M 33 or the star-forming regions in the SMC for the five regions of NGC 4214 presented in this paper. In regions I-1 and I-2, we find that the CO is broader by ~20%. Instead, in regions I-3, II, and III, the [C II] line is broader by ~60%. Although comparing the spectra does not directly show

massive differences in the CO and [C II] spectra, our decomposition showed that the [C II] emission is associated not only with CO, but also with H I. Studying dwarf galaxies in different tracers with *Herschel*, Cigan et al. (2016) also found that H I emission peaks correlate with [C II] peaks. We found that in region I the dominance (lowest value of (72 ± 13)% found in region I-1) of molecular mass is traced by [C II] rather than CO, implying extended CO-dark molecular gas. However, we note that the quoted values strongly depend on the assumed ISM conditions. Furthermore, we do not resolve the gas clouds spatially as the SOFIA/GREAT beam of 14″ corresponds to a spatial scale of about 200 pc.

Complementary to studies of low-metallicity environment, the origin of [C II] emission was also studied in the Milky Way. The Galactic Observations of Terahertz C$^+$ (GOTC$^+$; Yorke et al. 2010) comprises *Herschel*-HIFI [C II] observations of long lines of sight through the Galactic plane. It was found that the [C II] emission correlates with the star formation rate on galactic scales and that its emission can be divided into contributions from different ISM phases. They attribute 30% of the luminosity to dense PDRs, 25% to cold H I, 25% to CO-dark H$_2$, and 20% to ionized gas (Pineda et al. 2014). Velusamy & Langer (2014) combined GOTC+ [C II] data with ancillary H I and CO data to study the origin of Galactic [C II] emission. They found a widespread [C II] emission. About half of it is associated with diffuse molecular clouds faint in CO, but several lines of sight show features in either CO or H I without corresponding emission in [C II].

The star-forming region M 17 SW was studied by Pérez-Beaupuits et al. (2015) using spectrally resolved SOFIA/GREAT [C II] observations and by comparing them to [C I] and low-*J* CO lines. They analyzed their [C II] velocity channel maps with a different decomposition method and conclude that ~65% of the mass found with [C II] is not associated with star-forming material. The decomposition of the spectra implies that about 36%, 17%, and 47% of the [C II] emission originates from H II, H I, and H$_2$ regimes, respectively. Our study does not provide a comparison with a tracer of ionized gas, but previous studies showed that its contribution to the [C II] emission is low. Although there is large scatter, we find that we can associate about 46% of the [C II] emission on average with the H I emission.

6. Summary

We presented [C II] data observed with the GREAT instrument on board the SOFIA telescope in five regions of the low-metallicity irregular dwarf galaxy NGC 4214. The observations cover three separate regions in NGC 4214 in different evolutionary states. Star formation takes place in regions I and II whereas region III is considered less evolved with no star formation visible. We analyzed the velocity-resolved spectra by decomposing the [C II] emission spectra using ancillary H I and CO(2 → 1) data. We estimated gas masses associated with different ISM phases. We summarize our results as follows:

– The H I line profiles show almost the same widths of about 30 km s^{-1} in each of the five pointings and thus are broader than the [C II] lines by about 50% and broader than the CO lines by 20% in regions I-1 and I-2. In regions I-3 and II, the H I lines are more than twice as broad. All spectra peak at ~300 km s^{-1}, except for region III where the peaks are at ~280 km s^{-1}. The H I peak positions are shifted to slightly lower velocities in three regions compared to the [C II]. In

addition, the [C II] spectrum in this region is very noisy and thus difficult to decompose.

– Using Gaussian curves to fit the [C II], CO, and H I spectra we associate the majority (>70%) of the emission with the CO emission in regions I-1 and I-2. In region I-3, about 65% of the emission is attributed to the CO and in region II the fractions are split equally. On average, we can assign 54% of the [C II] emission to the CO emission.

– The gas mass of atomic hydrogen is about 10^6 $M_\odot$ in each of the five pointings, the molecular gas mass traced by CO is $\sim 2 \times 10^5$ $M_\odot$. This is only about 25% of the molecular mass seen in [C II]. The majority of molecular mass originates from CO-dark gas and between 32 and 87% of the total [C II] intensity originates from this material. These results agree with most other studies in nearby dwarf galaxies. We find the highest fraction of CO-dark molecular gas mass of (89 ± 10)% in region I-2 and it coincides with the position of a super star cluster. In region I, the most evolved star-forming region, we find an average CO-dark gas fraction of 84% while we find less CO-dark molecular gas (63%) in region II. This region is younger, more metal-rich and more compact. The fraction of CO-dark molecular gas is therefore sensitive to the evolutionary stage of the regions.

– Only about 9% of the total [C II] emission can be attributed to the CNM in agreement with the findings from Local Group galaxies. There are indications that the H I-associated [C II] also emits from denser phases. Similar to studies of the SMC and LMC, we find prominent wings in the [C II] profiles that cannot be fitted with CO spectra. The origin of these wings remains poorly constrained.

References

Bolatto, A. D., Wolfire, M., & Leroy, A. K. 2013, ARA&A, 51, 207
Braine, J., Combes, F., Casoli, F., et al. 1993, A&AS, 97, 887
Braine, J., Gratier, P., Kramer, C., et al. 2012, A&A, 544, A55
Cigan, P., Young, L., Cormier, D., et al. 2016, AJ, 151, 14
Cormier, D., Madden, S. C., Hony, S., et al. 2010, A&A, 518, L57
Cormier, D., Madden, S. C., Lebouteiller, V., et al. 2014, A&A, 564, A121
Cormier, D., Madden, S. C., Lebouteiller, V., et al. 2015, A&A, 578, A53
Dalcanton, J. J., Williams, B. F., Seth, A. C., et al. 2009, ApJS, 183, 67
Dimaratos, A., Cormier, D., Bigiel, F., & Madden, S. C. 2015, A&A, 580, A135
Gallagher, III, J. S., & Hunter, D. A. 1984, ARA&A, 22, 37
Genzel, R., & Cesarsky, C. J. 2000, ARA&A, 38, 761
Glover, S. C. O., & Mac Low, M.-M. 2011, in EAS Pub. Ser. 52, eds. M. Röllig, R. Simon, V. Ossenkopf, & J. Stutzki, 147
Goldsmith, P. F., Langer, W. D., Pineda, J. L., & Velusamy, T. 2012, ApJS, 203, 13
Grenier, I. A., Casandjian, J.-M., & Terrier, R. 2005, Science, 307, 1292
Guan, X., Stutzki, J., Graf, U. U., et al. 2012, A&A, 542, L4
Heiles, C., & Troland, T. H. 2003, ApJ, 586, 1067
Heyminck, S., Graf, U. U., Güsten, R., et al. 2012, A&A, 542, L1
Hollenbach, D. J., & Tielens, A. G. G. M. 1999, Rev. Mod. Phys., 71, 173
Hunter, D. A., Gallagher, III, J. S., Rice, W. L., & Gillett, F. C. 1989, ApJ, 336, 152
Israel, F. P. 1997, A&A, 328, 471
Kobulnicky, H. A., & Skillman, E. D. 1996, ApJ, 471, 211
Kulkarni, S. R., & Heiles, C. 1987, in Interstellar Processes, eds. D. J. Hollenbach, & H. A. Thronson, Jr., Astrophys. Space Sci. Libr., 134, 87

Langer, W. D., Velusamy, T., Pineda, J. L., Willacy, K., & Goldsmith, P. F. 2014, A&A, 561, A122
Leroy, A. K., Walter, F., Bigiel, F., et al. 2009, AJ, 137, 4670
MacKenty, J. W., Maíz-Apellániz, J., Pickens, C. E., Norman, C. A., & Walborn, N. R. 2000, AJ, 120, 3007
Madden, S. C., Poglitsch, A., Geis, N., Stacey, G. J., & Townes, C. H. 1997, ApJ, 483, 200
Maíz-Apellániz, J. 2001, ApJ, 563, 151
Maíz-Apellániz, J., Mas-Hesse, J. M., Munoz-Tunon, C., Vilchez, J. M., & Castaneda, H. O. 1998, A&A, 329, 409
Maíz-Apellániz, J., Muñoz-Tuñón, C., Tenorio-Tagle, G., & Mas-Hesse, J. M. 1999, A&A, 343, 64
Maíz-Apellániz, J., Cieza, L., & MacKenty, J. W. 2002, AJ, 123, 1307
McIntyre, V. J. 1997, PASA, 14, 122
Mookerjea, B., Kramer, C., Buchbender, C., et al. 2011, A&A, 532, A152
Narayanan, D., Krumholz, M., Ostriker, E. C., & Hernquist, L. 2011, MNRAS, 418, 664
Okada, Y., Requena-Torres, M. A., Güsten, R., et al. 2015, A&A, 580, A54
Pérez-Beaupuits, J. P., Stutzki, J., Ossenkopf, V., et al. 2015, A&A, 575, A9
Pilbratt, G. L., Riedinger, J. R., Passvogel, T., et al. 2010, A&A, 518, L1

Pineda, J. L., Langer, W. D., & Goldsmith, P. F. 2014, A&A, 570, A121
Planck Collaboration XIX. 2011, A&A, 536, A19
Poglitsch, A., Krabbe, A., Madden, S. C., et al. 1995, ApJ, 454, 293
Poglitsch, A., Waelkens, C., Geis, N., et al. 2010, A&A, 518, L2
Requena-Torres, M. A., Israel, F. P., Okada, Y., et al. 2016, A&A, 589, A28
Schruba, A., Leroy, A. K., Walter, F., et al. 2012, AJ, 143, 138
Sellwood, J. A., & Balbus, S. A. 1999, ApJ, 511, 660
Stacey, G. J., Geis, N., Genzel, R., et al. 1991, ApJ, 373, 423
Tamburro, D., Rix, H.-W., Leroy, A. K., et al. 2009, AJ, 137, 4424
Thurow, J. C., & Wilcots, E. M. 2005, AJ, 129, 745
Úbeda, L., Maíz-Apellániz, J., & MacKenty, J. W. 2007a, AJ, 133, 917
Úbeda, L., Maíz-Apellániz, J., & MacKenty, J. W. 2007b, AJ, 133, 932
Velusamy, T., & Langer, W. D. 2014, A&A, 572, A45
Walter, F., Taylor, C. L., Hüttemeister, S., Scoville, N., & McIntyre, V. 2001, AJ, 121, 727
Walter, F., Brinks, E., de Blok, W. J. G., et al. 2008, AJ, 136, 2563
Wolfire, M. G., Hollenbach, D., & McKee, C. F. 2010, ApJ, 716, 1191
Yorke, H., Langer, W., Velusamy, T., et al. 2010, in COSPAR Meeting, 38th COSPAR Scientific Assembly, 38, 2482
Young, E. T., Becklin, E. E., Marcum, P. M., et al. 2012, ApJ, 749, L17

Appendix A: Decomposition: Channel method

A.1. Description of the method

In conjunction with the decomposition method described in Sect. 3 that uses Gaussians to fit the spectra, we also used the CO and H I spectra directly. For each region, we want to describe our [C II] spectra S by a linear combination of CO and H I:

$$S_{\mathrm{syn,[C\,II]}} = a\,S_{\mathrm{H\,I}} + b\,S_{\mathrm{CO}}. \tag{A.1}$$

This method shows some similarities with the approach that was used by Pérez-Beaupuits et al. (2015) to study the origin of [C II] in M17 SW.

To compute the synthetic spectra, we first normalize the CO and H I spectra by their maximum and then choose the coefficients as percentages so that the CO and H I spectra add up to 100%. A percentage X means that the whole H I spectrum is multiplied by this number and then added to the CO spectrum multiplied correspondingly with 100-X%. In an ideal case, this combined synthetic spectrum would peak at the same flux density as the [C II] spectra. However, the best decomposition result might be achieved, if the synthetic spectra peaks at a slightly different flux density. Therefore, we introduce the scaling parameter k, where $k = 100$% corresponds to a scaling to the height of the [C II] peak. Equation (A.1) now reads

$$S_{\mathrm{syn,[C\,II]}} = k \max(S_{\mathrm{[C\,II]}}) \left(X \frac{S_{\mathrm{H\,I}}}{\max(S_{\mathrm{H\,I}})} + (100 - X) \frac{S_{\mathrm{CO}}}{\max(S_{\mathrm{CO}})} \right). \tag{A.2}$$

To quantify the quality of a decomposition with H I percentage X and scaling factor k, we compute the residual by subtracting the synthetic from the original [C II] spectrum. The standard deviation of the residual is then used to measure the quality of this decomposition.

This procedure is repeated for all possible values of X with integer percentages and scale factors ranging from 75% to 100% for each percentage. For our best decomposition we want a low standard deviation of the residual and a high scaling factor k. To achieve the latter, we do not consider values of k below 75% since we want to reproduce the peak. We then vary the percentages X and scaling factors k and take the (X, k) pair with minimum residual (see Fig. A.1). In this example for region II, $X = 40$% and $k = 100$.

However, this approach can result in residuals with broad negative features that would correspond to emission not seen in the [C II] spectra. These features are created mostly for high H I percentages as the H I spectra are broader than the [C II] spectra.

We filter out decompositions with these negative features by rejecting all parameter pairs (X, k) that result in residuals with more than three consecutive velocity channels below a certain threshold. For each pointing, this threshold is determined by the highest noise level of the [C II], CO(2 → 1), and H I spectra after scaling. While the RMS of the combined spectra depends on the CO and H I spectra, the noise in the [C II] also sets a limitation for finding the best decomposition. We find that the best results are obtained when the threshold is set to 1σ rms of the noise.

Using this approach, we can find parameter sets of X and k that give a decomposition for our five [C II] spectra. However, sometimes it is necessary to adjust the parameters manually,
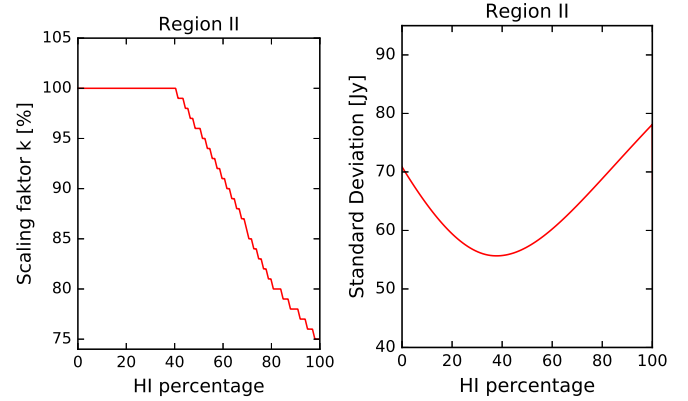
Fig. A.1. *First panel*: scale factor k that provides the lowest standard deviation of the residual versus the H I percentage X in region II. *Second panel*: standard deviation versus H I percentage. The minimum obtained for an H I percentage of 37% and a scaling factor of 100%.

typically within 10%, in order to get the best-matching synthetic spectrum. This range reflects the uncertainty of our channel decomposition method.

A.2. Results

Table A.1 reports the best results of the channel method decomposition. We note that the uncertainty of the H I percentages are around 10%. The CO(2 → 1) are 100% minus the H I percentages. We also note that the CO percentage factor is higher in all pointings. The [C II] line profile is more closely associated with the CO(2 → 1) emission than with the broader H I spectra, as was also seen in the Gaussian fit method. Table A.1 also lists the [C II] intensity fractions associated with CO and H I. These values were calculated by direct integration of the [C II] and the scaled CO and H I spectra.

Figure A.2 presents the final decomposition of our [C II] spectra with the corresponding residuals. The decomposition works best for region I-1 and region II where the weighted spectra of H I and CO reproduce the shape of the [C II] well. Region III shows a flat residual, but here the best fitting decomposition does not match well owing to the broad, uneven line shape. In this region, it is questionable whether the [C II] emission is strong enough to be decomposed in a useful manner. The decomposition of [C II] in region I-3 looks reasonable, although the residual shows a significant dip at ~290 km s^{-1}. We note that it was not possible to reduce this dip any further. The decomposition is worst in region I-2. The weighted spectrum shows side features and has a broad top with two peaks.

Overall, the weighted and scaled spectra of H I and CO(2 → 1) can account for most [C II] emission at least reasonably well. We find no strong indication for components in the observed regions that are not visible in either H I or CO, but are visible in [C II].

When comparing the results to those of the Gaussian method (see Table 3), we find no significant differences. However, we prefer the Gaussian fitting method because it enables us to fit several components in the H I spectra. In addition, the channel method requires manual tuning to find the best parameter set for the synthetic [C II] spectrum.

Table A.1. Results from the channel method decomposition.

Region	H I	CO(2 → 1)	k	$I_{\text{[C II]}}(\text{H I})/I_{\text{[C II]}}$	$I_{\text{[C II]}}(\text{CO})/I_{\text{[C II]}}$
I-1	40%	60%	80%	55.0%	44.1%
I-2	35%	65%	75%	47.8%	61.9%
I-3	45%	55%	98%	70.6%	28.7%
II	25%	75%	100%	40.4%	61.9%
III	30%	70%	75%	37.5%	39.1%

Notes. Intensity fractions $I_{\text{[C II]}}(\text{H I})/I_{\text{[C II]}}$ and $I_{\text{[C II]}}(\text{CO})/I_{\text{[C II]}}$ using the scaled H I and CO spectra.
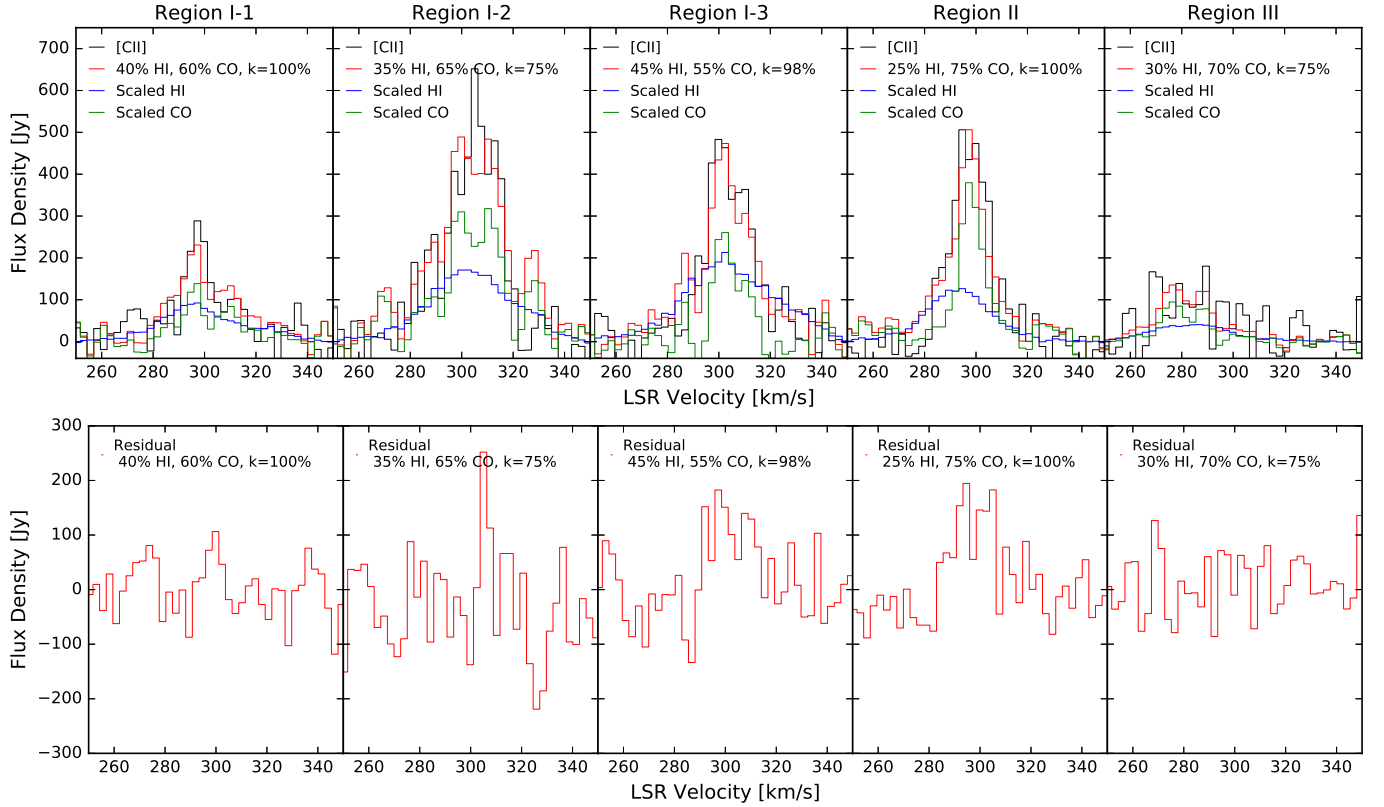
Fig. A.2. Channel method decomposition. *Upper row*: original [C II] spectra in black and the best fitting synthetic spectra in red with the weightings given in Table A.1. The accordingly scaled H I spectra are shown in blue, CO(2 → 1) in green. *Bottom row*: residuals computed from the weighted spectra by subtraction from [C II] data.